Mathematical Modeling of Rubber Elasticity

Hiroshi Koibuchi, Chrystelle Bernard, Jean-Marc Chenal, Gildas Diguet, Gaël Sebald, Jean-Yves Cavaillé, Toshiyuki Takagi, Laurent Chazeau

Mathematical Modeling of Rubber Elasticity

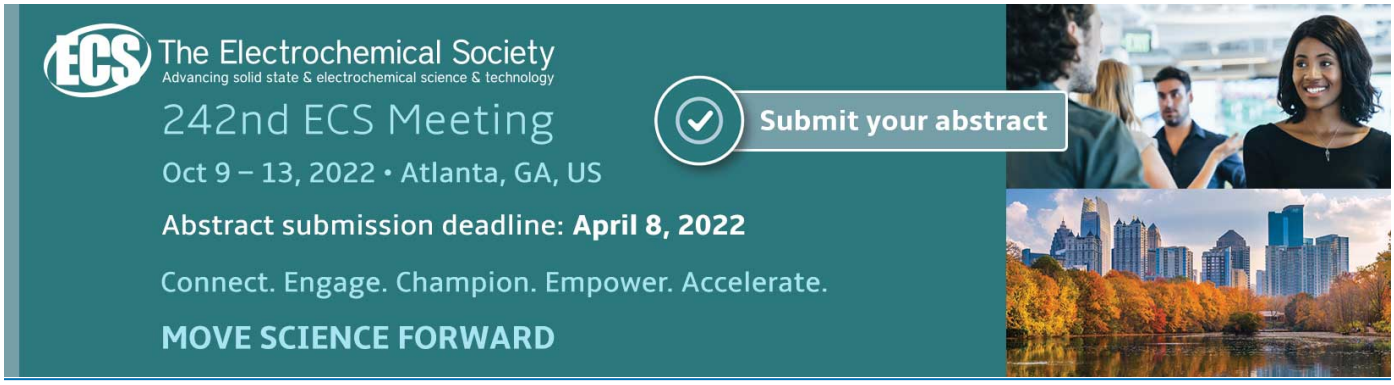

IOP Conf. Series: Journal of Physics: Conf. Series 1141 (2018) 012081 doi:10.1088/1742-6596/1141/1/012081

Mathematical Modeling of Rubber Elasticity

Hiroshi Koibuchi[a,1], Chrystelle Bernard[b,c], Jean-Marc Chenal[d], Gildas Diguet[b], Gael Sebald[b], Jean-Yves Cavaille[b,2], Toshiyuki Takagi[b,e], and Laurent Chazeau[d]

[a]National Institute of Technology, Ibaraki College, Nakane 866, Hitachinaka, Ibaraki 312-8508, Japan;
[b]ELyTMaX UMI 3757, CNRS-Universite de Lyon, Tohoku University, International Joint Unit, Tohoku University, 2-1-1 Katahira, Aoba-ku, Sendai, 980-8577, Japan;
[c]Frontier Research Institute for Interdisciplinary Sciences (FRIS), Tohoku University, 6-3 Aoba Aramaki, Aoba-ku, Sendai, Miyagi 980-8578, Japan;
[d]Materials Engineering and Science (MATEIS), CNRS, INSA Lyon UMR 5510, Université de Lyon Batiment B. Pascal, Avenue Jean Capelle, 69621 Villeurbanne Cedex, France;
[e]Institute of Fluid Science (IFS), Tohoku University, 2-1-1 Katahira, Aoba-ku Sendai, Miyagi 980-0812, Japan

E-mail: [1]koibuchih@gmail.com; [2]jean-yves.cavaille@insa-lyon.fr

A mathematical modeling, the Finsler geometry (FG) technique, is applied to study the rubber elasticity. Existing experimental data of stress-strain (SS) diagrams, which are highly non-linear, are numerically reproduced. Moreover, the strain induced crystallization (SIC), typical of some rubbers like Natural Rubber (NR), which is known to play an important role in the mechanical property of rubbers, is partly implemented in the model. Indeed, experimentally observed hysteresis of SS curve can be reproduced if the parameter a of non-polar (or polar) interaction energy is increased for the unloading or shrinkage process in the Monte Carlo (MC) simulations, and at the same time we find that the order parameter M of the directional degrees of freedom σ of polymer show a hysteresis behavior which is compatible with that of the crystallization ratio. In addition, rupture phenomena, which are accompanied by a necking phenomenon observed in the plastic deformation region, can also be reproduced. Thus we find that the interaction implemented in the FG model via the Finsler metric is suitable in describing the mechanical property of rubbers.
Keywords: *Rubber elasticity, Natural rubber, Stress-strain diagram, Strain induced crystallization, Necking of rubber, Finsler geometry*

1. Introduction

The main specific feature of Natural Rubber is that it crystallizes when stretched above an elongation of about 3 (see Figs.1(a),(b)) [1, 2, 3, 4]. This makes it extremely resilient against tearing as near the rupture tip, local strain induces crystallization which in turn slows down the tear propagation. As it is an almost unique behavior for rubber, NR is widely used to manufacture truck tires, representing a huge industrial market. Figure 1(c) schematically illustrates such behavior.

In the FG modeling for studying the mechanical property of materials, we modify the geometric structure inside the material simply by replacing the Euclidean metric with Finsler

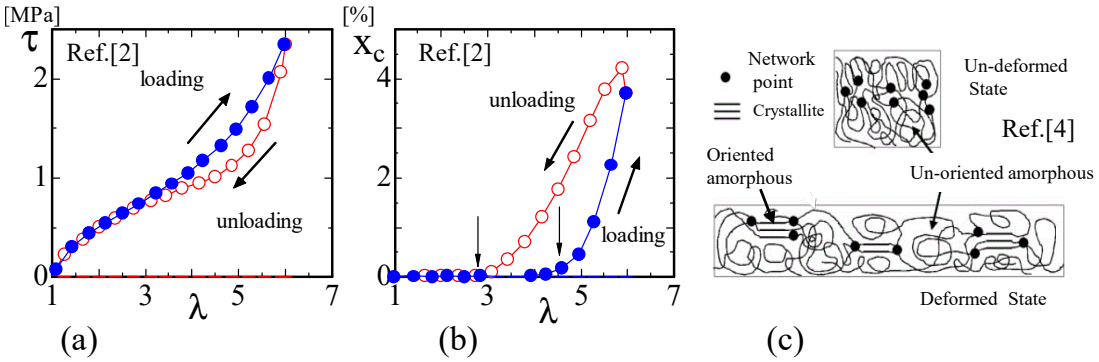

Figure 1. (a) The stress τ vs. elongation ratio $\lambda(= L/L_0)$, (b) the crystalline fraction vs. λ for loading and unloading processes (from [2]), and (c) illustrations of polymer structure in deformed and undeformed states (from [4]).

metric. As a result of this geometry modification, the interaction is effectively introduced between the directional and positional degrees of freedom of polymers [5]. Therefore, this technique is new and completely different from the ordinary modeling techniques. The FG modeling technique was already successfully applied to several interesting phenomena: the so-called soft elasticity observed in the liquid crystal elastomers as a response to external mechanical forces, the elongations under the temperature change [6] and by electric field [7], and shape deformation of LCE piece under light irradiation [8]. It was also shown that the J-shaped SS curve of biological materials such as animal skin and muscle is calculated by 2D and 3D FG models [9, 10]. Moreover, the origin of the line tension energy, which plays an important role in the model of two-component membranes, is explained by a 2D FG model [11]. These results enable us to consider that FG model can also be applied to rubber elasticity.

2. Models

2.1. 3D Model

The continuous Hamiltonian for 3D model is given by

$$S_1 = \int \sqrt{g} d^3x g^{ab} \frac{\partial \mathbf{r}}{\partial x_a} \cdot \frac{\partial \mathbf{r}}{\partial x_a}, \quad S_2 = \int \sqrt{g} d^3x \left(g^{ab} \frac{\partial \mathbf{r}}{\partial x_a} \cdot \frac{\partial \mathbf{r}}{\partial x_a} \right)^2 \tag{1}$$

where $\mathbf{r}(\in \mathbf{R}^3)$ is a function of the parameters $x_a (a = 1, 2, 3)$ as the position of 3D material, g is the determinant of 3×3 matrix g_{ab}, and g^{ab} is its inverse. S_1 is the so-called Gaussian bond potential, while S_2 is a simple extension of S_1 and quadratic with respect to $\partial \mathbf{r}/\partial x_a$.

Here we describe the outline of the 3D FG model. Two-dimensional cylinder with finite thickness, discretized by tetrahedrons, are used to define the discrete Hamiltonian (Fig. 2(a)). On the tetrahedron with vertices 1234 (Fig. 2(b)), the discrete metric g_{ab} is given by [5, 6]

$$g_{ab} = \begin{pmatrix} 1/v_{12}^2 & 0 & 0 \\ 0 & 1/v_{13}^2 & 0 \\ 0 & 0 & 1/v_{14}^2 \end{pmatrix}. \tag{2}$$

In this discrete metric, the Finsler length v_{ij} is defined by

$$v_{ij} = \begin{cases} |\mathbf{t}_{ij} \cdot \sigma_i| + v_0 & \text{(model 1)} \\ \sqrt{1 - |\mathbf{t}_{ij} \cdot \sigma_i|^2} + v_0 & \text{(model 2)} \end{cases}, \quad \mathbf{t}_{ij} = \vec{\ell}_{ij}/\ell_{ij}, \ \vec{\ell}_{ij} = \mathbf{r}_j - \mathbf{r}_i \tag{3}$$

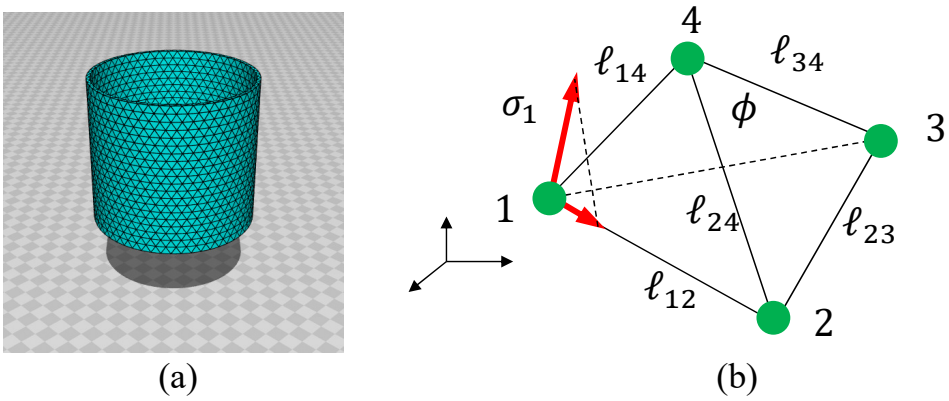

Figure 2. (a) A cylinder composed of tetrahedra for 3D model, (b) a tetrahedron with vertices 1234, and the variable σ_1 with its tangential component along the edge 12.

where σ_i corresponds to the polymer direction at the vertex i, and $v_0(=0.001)$ in v_{ij} is the cutoff.

Replacing the integral with the finite sum $\int \sqrt{g} d^3x \to \sum_\Delta v_{12}^{-1} v_{13}^{-1} v_{14}^{-1}$ and the differentials with the differences $\partial_1 \mathbf{r} \to \mathbf{r}_2 - \mathbf{r}_1, \partial_2 \mathbf{r} \to \mathbf{r}_3 - \mathbf{r}_1, \partial_3 \mathbf{r} \to \mathbf{r}_4 - \mathbf{r}_1$ in Eq.(1), and including the other symmetric terms obtained by the replacements $1 \to 2$, $2 \to 3$, $3 \to 4$, $4 \to 1$, we have the discrete S_1 and S_2. In this discretization, four symmetric terms are summed over with the factor $1/4$. Including several additional terms, we have the Hamiltonian [10]:

$$
\begin{aligned}
&S(\mathbf{r},\sigma) = aS_0(\sigma) + bS_1(\mathbf{r},\sigma) + cS_2(\mathbf{r},\sigma) + \kappa S_3(\mathbf{r}) + U_{3D}(\mathbf{r}) + U_B, \\
&S_0(\sigma) = \frac{1}{2}\sum_{ij}\left(1 - 3(\sigma_i \cdot \sigma_j)^2\right), \\
&S_1 = \sum_{ij} \Gamma_{ij} \ell_{ij}^2, \ \Gamma_{ij} = \frac{1}{\bar{N}} \sum_{\text{tet}} \gamma_{ij}(\text{tet}), \ \ell_{ij}^2 = (\mathbf{r}_i - \mathbf{r}_j)^2, \\
&S_2(\sigma) = \sum_{ij} \Gamma_{ij}^{(1)} \ell_{ij}^4 + \sum_{ij,kl} \Gamma_{ij,kl}^{(2)} \ell_{ij}^2 \ell_{kl}^2, \quad S_3(\mathbf{r}) = \sum_i \left[1 - \cos(\phi_i - \pi/3)\right], \\
&U_{3D}(\mathbf{r}) = \sum_{\text{tet}} U_{3D}(\text{tet}), \quad U_{3D}(\text{tet}) = \begin{cases} 0 & (\text{Vol(tet)} > 0) \\ \infty & (\text{otherwise}) \end{cases}, \\
&U_B = \sum_{i \in \text{boundary}} U_B(\mathbf{r}_i), \quad U_B(\mathbf{r}_i) = \begin{cases} \infty & (|z_i - H| > \delta_B \text{ or } |z_i| > \delta_B) \\ 0 & (\text{otherwise}) \end{cases}.
\end{aligned}
\tag{4}
$$

The first term aS_0 is the Lebwohl-Lasher potential for LC molecules with the interaction coefficient a. The second and third terms S_1 and S_2 are discrete versions of the terms in Eq. (1). In the coefficient Γ_{ij} of the second term bS_1, the symbol $\bar{N}$ is given by

$$
\bar{N} = (1/N_B) \sum_{ij} n_{ij}, \tag{5}
$$

where n_{ij} is the total number of tetrahedra sharing the bond ij and $N_B(=\sum_{ij} 1)$ is the total number of bonds. The coefficients $\gamma_{ij}(=\gamma_{ji})$ in Γ_{ij} are defined as

$$
\begin{aligned}
&\gamma_{12} = \frac{1}{4}\left(\frac{v_{12}}{v_{13}v_{14}} + \frac{v_{21}}{v_{23}v_{24}}\right), \ \gamma_{13} = \frac{1}{4}\left(\frac{v_{13}}{v_{12}v_{14}} + \frac{v_{31}}{v_{32}v_{34}}\right), \ \gamma_{14} = \frac{1}{4}\left(\frac{v_{14}}{v_{12}v_{13}} + \frac{v_{41}}{v_{42}v_{43}}\right), \\
&\gamma_{23} = \frac{1}{4}\left(\frac{v_{23}}{v_{21}v_{24}} + \frac{v_{32}}{v_{31}v_{34}}\right), \ \gamma_{24} = \frac{1}{4}\left(\frac{v_{24}}{v_{21}v_{23}} + \frac{v_{42}}{v_{41}v_{43}}\right), \ \gamma_{34} = \frac{1}{4}\left(\frac{v_{34}}{v_{31}v_{32}} + \frac{v_{43}}{v_{41}v_{42}}\right),
\end{aligned}
\tag{6}
$$

where v_{ij} are defined on the tetrahedron in Fig. 2(b) and $\sum_{\rm tet}$ denotes the sum over tetrahedra, each of which shares the bond ij.

In the third term cS_2, the coefficients $\Gamma^{(1)}_{ij}$ and $\Gamma^{(2)}_{ij,kl}$ on the tetrahedron in Fig. 2(b) are given by

$$\begin{aligned}
\Gamma^{(1)}_{12} &= \frac{1}{6}\left(\frac{v_{12}^3}{v_{13}v_{14}}+\frac{v_{21}^3}{v_{23}v_{24}}\right), \quad \Gamma^{(1)}_{13} = \frac{1}{6}\left(\frac{v_{13}^3}{v_{12}v_{14}}+\frac{v_{31}^3}{v_{32}v_{34}}\right),\\
\Gamma^{(1)}_{14} &= \frac{1}{6}\left(\frac{v_{14}^3}{v_{12}v_{13}}+\frac{v_{41}^3}{v_{42}v_{43}}\right), \quad \Gamma^{(1)}_{23} = \frac{1}{6}\left(\frac{v_{23}^3}{v_{21}v_{24}}+\frac{v_{32}^3}{v_{31}v_{34}}\right),\\
\Gamma^{(1)}_{24} &= \frac{1}{6}\left(\frac{v_{24}^3}{v_{21}v_{23}}+\frac{v_{42}^3}{v_{41}v_{43}}\right), \quad \Gamma^{(1)}_{34} = \frac{1}{6}\left(\frac{v_{34}^3}{v_{31}v_{32}}+\frac{v_{43}^3}{v_{41}v_{42}}\right)
\end{aligned} \tag{7}$$

and

$$\begin{aligned}
\Gamma^{(2)}_{12,13} &= \frac{1}{3}\frac{v_{12}v_{13}}{v_{14}}, \quad \Gamma^{(2)}_{12,14} = \frac{1}{3}\frac{v_{12}v_{14}}{v_{13}}, \quad \Gamma^{(2)}_{13,14} = \frac{1}{3}\frac{v_{13}v_{14}}{v_{12}},\\
\Gamma^{(2)}_{21,23} &= \frac{1}{3}\frac{v_{21}v_{23}}{v_{24}}, \quad \Gamma^{(2)}_{23,24} = \frac{1}{3}\frac{v_{23}v_{24}}{v_{21}}, \quad \Gamma^{(2)}_{21,24} = \frac{1}{3}\frac{v_{21}v_{24}}{v_{23}},\\
\Gamma^{(2)}_{31,32} &= \frac{1}{3}\frac{v_{31}v_{32}}{v_{34}}, \quad \Gamma^{(2)}_{31,34} = \frac{1}{3}\frac{v_{31}v_{34}}{v_{32}}, \quad \Gamma^{(2)}_{32,34} = \frac{1}{3}\frac{v_{32}v_{34}}{v_{31}},\\
\Gamma^{(2)}_{41,42} &= \frac{1}{3}\frac{v_{41}v_{42}}{v_{43}}, \quad \Gamma^{(2)}_{41,43} = \frac{1}{3}\frac{v_{41}v_{43}}{v_{42}}, \quad \Gamma^{(2)}_{42,43} = \frac{1}{3}\frac{v_{42}v_{43}}{v_{41}}.
\end{aligned} \tag{8}$$

We should note that $\Gamma^{(1)}_{ij}=\Gamma^{(1)}_{ji}$ and $\Gamma^{(2)}_{ij,kl}=\Gamma^{(2)}_{kl,ij}$ for all possible combinations of ij and kl.

The symbol ϕ_i in the fourth term κS_3 is an internal angle of triangle, and this term κS_3 is the deformation energy of tetrahedron with the constant κ, which represents deformation strength against bending, shear and tensile deformation excluding simple expansion/shrinkage. This term plays a role of maintaining the shape of 3D body. The fifth term U_{3D} protects the tetrahedron volume from being negative.

The potential U_B allows the boundary vertices to move vertically in the height direction within a small range $\pm\delta_B$, which is fixed to the mean bond length. This constraint does not influence the results in the limit of $N\to\infty$ because δ_B/H is negligible in this limit

$$\frac{\delta_B}{H}\left(=\frac{\text{mean bond length}}{\text{height of cylinder}}\right)\to 0 \quad (N\to\infty), \tag{9}$$

because the mean bond length is independent of N, while H is proportional to N. The reason why this constraint U_B is assumed to be avoiding a strong and non-physical force, which is suspected to appear when σ_i aligns with the height direction on the boundary for $\delta_B = 0$.

2.2. 2D Model

The continuous energies assumed in 2D model are

$$\begin{aligned}
S_1 &= \int \sqrt{g}d^2x g^{ab}\frac{\partial \mathbf{r}}{\partial x_a}\cdot\frac{\partial \mathbf{r}}{\partial x_a}, \quad S_2 = \int \sqrt{g}d^2x \left(g^{ab}\frac{\partial \mathbf{r}}{\partial x_a}\cdot\frac{\partial \mathbf{r}}{\partial x_a}\right)^2,\\
S_3 &= \frac{1}{2}\int \sqrt{g}d^2x g^{ab}\frac{\partial \mathbf{n}}{\partial x_a}\cdot\frac{\partial \mathbf{n}}{\partial x_a}.
\end{aligned} \tag{10}$$

The first two terms S_1 and S_2 are identical with those of Eq. (1) except the integration $\int\sqrt{g}d^dx$, where $d=3$ ($d=2$) for 3D (2D) model. The third term S_3 is the continuous bending energy of

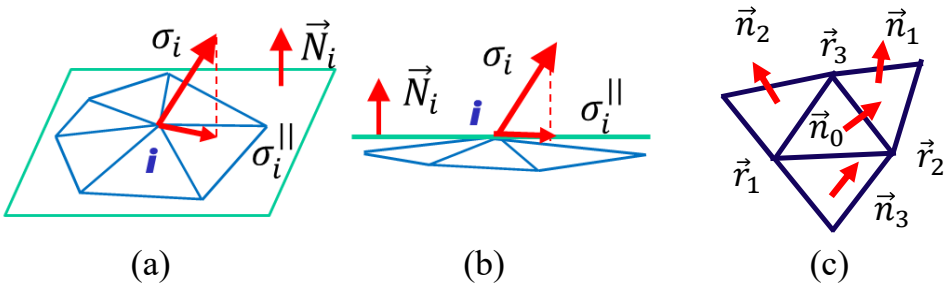

Figure 3. (a), (b) The tangential plane at the vertex i, its normal vector $\mathbf{N}_i$, and the variable σ_i, for 2D model, (c) normal vectors $\mathbf{n}_i (i = 0, 1, 2, 3)$ of the triangle 123 and three neighboring triangles.

the cylindrical surface, and $\mathbf{n}$ is a unit normal vector of the surface. This term S_3 correspond to the deformation energy S_3 of 3D model in Eq. (4), although S_3 for 2D model has only resistance against bending deformation.

The discrete Hamiltonian of the 2D model is given by a linear combination of four different terms such that [10]

$$\begin{aligned} &S(\sigma, \mathbf{r}) = aS_0 + bS_1 + cS_2 + \kappa S_3 + U_B, \quad (\gamma = 1), \\ &S_0(\sigma) = -(3/2) \sum_{ij} \left(\sigma_i^{||} \cdot \sigma_j^{||} \right)^2, \\ &S_1 = \sum_{ij} \gamma_{ij} \ell_{ij}^2, \quad S_2(\sigma) = \sum_{ij} \Gamma_{ij}^{(1)} \ell_{ij}^4 + \sum_{ij,kl} \Gamma_{ij,kl}^{(2)} \ell_{ij}^2 \ell_{kl}^2, \\ &S_3 = \sum_{\Delta} \left[\kappa_{12} \left(1 - \mathbf{n}_0 \cdot \mathbf{n}_3 \right) + \kappa_{23} \left(1 - \mathbf{n}_0 \cdot \mathbf{n}_1 \right) + \kappa_{31} \left(1 - \mathbf{n}_0 \cdot \mathbf{n}_2 \right) \right]. \end{aligned} \tag{11}$$

The variable $\sigma_i^{||}$ in S_0 is defined by

$$\sigma_i^{||} = \sigma_i - (\sigma_i \cdot \mathbf{N}_i) \mathbf{N}_i, \tag{12}$$

which is a component of σ_i parallel to the tangential plane at the vertex i (Figs. 3(a),(b)). This tangential plane is determined by its unit normal vector $\mathbf{N}_i$, which is defined such that

$$\mathbf{N}_i = \frac{\sum_{j(i)} A_{j(i)} \mathbf{n}_{j(i)}}{\left| \sum_{j(i)} A_{j(i)} \mathbf{n}_{j(i)} \right|}, \tag{13}$$

where $A_{j(i)}$ and $\mathbf{n}_{j(i)}$ denote the area and the unit normal vector of the triangle $j(i)$ sharing the vertex i, respectively (Figs. 3(a),(b)).

The coefficients $\gamma_{ij} (= \gamma_{ji})$ in S_1 and $\Gamma_{ij}^{(1)} (= \Gamma_{ji}^{(1)})$, $\Gamma_{ij,kl}^{(2)} (= \Gamma_{kl,ij}^{(2)})$ in S_2 of 2D model are different from those of 3D model, and these are defined by

$$\begin{aligned} &\gamma_{12} = \frac{1}{6} \left(\frac{v_{12}}{v_{13}} + \frac{v_{21}}{v_{23}} \right), \quad \gamma_{23} = \frac{1}{6} \left(\frac{v_{23}}{v_{21}} + \frac{v_{32}}{v_{31}} \right), \quad \gamma_{31} = \frac{1}{6} \left(\frac{v_{31}}{v_{32}} + \frac{v_{13}}{v_{12}} \right), \\ &\Gamma_{12}^{(1)} = \frac{1}{6} \left(\frac{v_{12}^3}{v_{13}} + \frac{v_{21}^3}{v_{23}} \right), \quad \Gamma_{23}^{(1)} = \frac{1}{6} \left(\frac{v_{23}^3}{v_{21}} + \frac{v_{32}^3}{v_{31}} \right), \quad \Gamma_{31}^{(1)} = \frac{1}{6} \left(\frac{v_{31}^3}{v_{32}} + \frac{v_{13}^3}{v_{12}} \right), \\ &\Gamma_{12,13}^{(2)} = \frac{1}{3} v_{12} v_{13}, \quad \Gamma_{21,23}^{(2)} = \frac{1}{3} v_{21} v_{23}, \quad \Gamma_{31,32}^{(2)} = \frac{1}{3} v_{31} v_{32} \end{aligned} \tag{14}$$

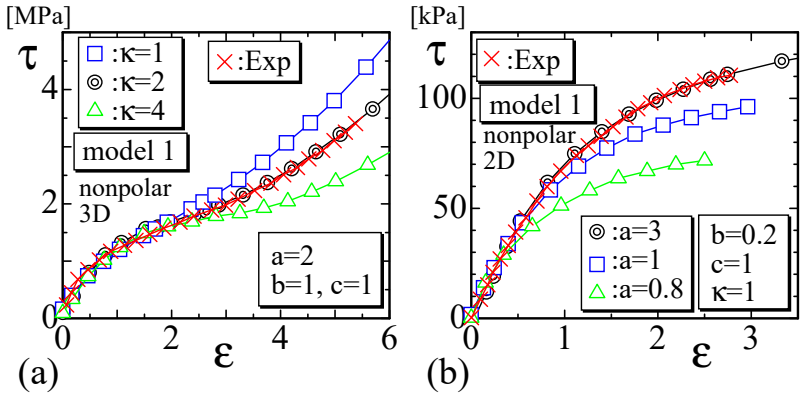

Figure 4. The stress τ vs. strain $\varepsilon(=\lambda-1)$ for (a) Exp data for EPDM/LDH (Layered double hydroxides (LDHs) based elastomer nanocomposite) [12] and the simulation data of 3D model, (b) Exp data for untreated cotton fiber composite [13] and the simulation data of 2D model.

on the triangle 123 (Fig. 3(c)), where the vertex position is given by $\mathbf{r}_i, (i=1,2,3)$, and v_{ij} is defined by the same expression as that in Eq.(3). The coefficients $\kappa_{ij}(=\kappa_{ji})$ of S_3 are given by

$$\kappa_{12}=\frac{1}{6}\left(\frac{v_{13}}{v_{12}}+\frac{v_{23}}{v_{21}}\right), \quad \kappa_{23}=\frac{1}{6}\left(\frac{v_{21}}{v_{23}}+\frac{v_{31}}{v_{32}}\right), \quad \kappa_{31}=\frac{1}{6}\left(\frac{v_{32}}{v_{31}}+\frac{v_{12}}{v_{13}}\right). \tag{15}$$

on the triangle 123. The potential U_B is the same as for 3D model, and hence the definition of U_B is not written in Eq. (11). The discrete unit normal vectors $\mathbf{n}_0$ and $\mathbf{n}_i(i=1,2,3)$ are defined on the triangle 123 and its neighboring triangles shown in Fig. 3(c).

3. Calculation of tensile stress

The nominal surface tension (or frame tension) is given by

$$\tau=\frac{2\langle S_1\rangle-3N+4N_1}{2A_{\rm p}}, \quad A_{\rm p}=\pi D_0 H, \tag{16}$$

where D_0 is the diameter of the boundary and N_1 is the total number of boundary vertices. We should note that $A_0=\pi D_0^2$, where the initial height is given by $H=D_0$ [10]. This formula is obtained by the so-called scale invariance of the partition function.

To compare the frame tension τ with the experimentally observed stress, we have to change the unit of $\tau[1/k_BT]$ by using the lattice spacing a[1/m]. We have

$$\tau_{\rm sim}=\frac{k_BT}{a^3}\tau=\left(\frac{4\times10^{-21}}{a^3}\right)\tau\ [{\rm N/m^2}], \tag{17}$$

where the value of a can be varied to modify the simulation data τ, and the modified $\tau_{\rm sim}$ can be compared to the experimentally observed stress $\tau_{\rm exp}$ [10]. The only constraint for a is that a should be larger than Van der Waals distance, this is always satisfied in our calculations.

4. Monte Carlo results and discussions

Figure 4(a) shows an experimental stress-strain diagram ($\times$) [12] and the MC data (other symbols) of 3D model with the variation of κ, and Fig. 4(b) shows the Exp data [13] and the MC data of 2D model. We find that one of the simulation data is in good agreement with

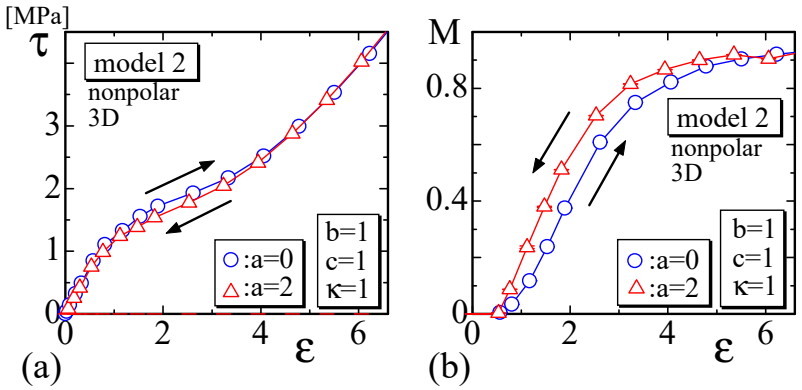

Figure 5. (a) The SIC simulation data τ vs. ϵ of 3D model, and (b) the corresponding order parameter M vs. ε. The symbol $\nearrow$ ($\swarrow$) indicates loading (unloading) process in experiments, though the simulation at each point is performed independently of those at other points.

the Exp data in both Figs. 4(a) and 4(b). Here we use symbol τ for the stress, because the commonly used symbol σ is already used for the direction of polymers.

The SS curves are in general measured in time-dependent extension/shrinkage experiments, and the SIC is reflected in the curves as hysteresis as shown in Fig. 1(a) [1, 2]. The SS curve for the shrinkage process is always below the curve of the first extension process. During SIC process, the internal structure of rubber partly changes as a phase transition between the random to crystalline phases, and hence the hysteresis can be observed in this region. In this sense, the SIC is understood as an equilibrium phenomenon. Therefore, the SIC can be understood in the framework of statistical mechanics.

However, the problem is that the experiments are always performed within a time much shorter than the time expected from the relaxation time. We should emphasize that the hysteresis in SS curves during extension/shrinkage experiments is unable to obtain by any MC simulations with the parameters identical for loading and unloading processes. This is the reason why we change parameters for the MC simulations loading and unloading processes. In those simulations, we simply assume two different equilibrium states characterized by the difference in parameters for the two processes.

Here, we should remind that this crystallization ratio is physically close to the order parameter $M=(3/2)\,(\langle\sigma_z^2\rangle-1/3)$ (nonpolar) though the concrete relation is unknown at present, and that M can be controlled by the coefficient a for S_0 in the FG model. From these considerations, we fix a in the extension and shrinkage processes such that $a=0$ (ext) and $a=2$ (shr), for example. Thus, we see a "hysteresis" of τ in Fig. 5(b) and M in Fig. 5(c). We should note that these are not "hysteresis" but are equilibrium simulation data obtained with different a's. The arrows simply indicate that the data correspond to experimental "hysteresis" data (though experimental data are not plotted).

In addition, we show that a rupture phenomenon (RP) observed for sufficiently large ε can be simulated in the FG modeling. This phenomenon is characterized by a sudden drop of the stress τ, and it is well-known that a necking phenomenon appears just before the break into two parts. In Fig.6(a), experimental data ($\times$) [14] with simulation data (other symbols) are plotted, and the simulation data τ for $a=0$ discontinuously change at large strain region. This change of τ is considered as an RP, although τ remains non-zero after the "break", which is not a real break but always "connected" in the model. The oder parameter M also discontinuously changes. "Necking phenomenon" can be seen in the snapshot in Fig.6(c).

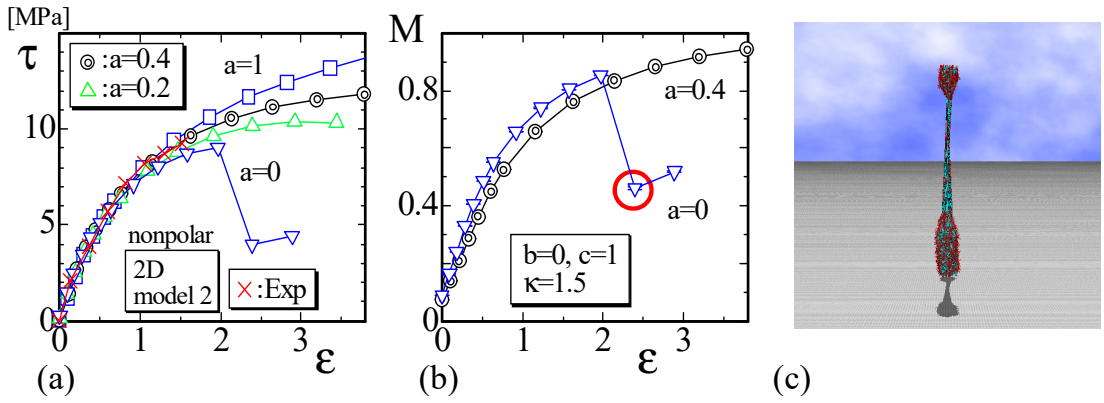

Figure 6. (a) τ vs. $\varepsilon(=\lambda-1)$ of Exp data for dry Nafion-H^+ membrane at 150 ° [14] and simulation data of 2D model, (b) M vs. ε of the simulation data under $a=0$ and $a=0.4$, (c) a snapshot corresponding to the point encircled (◯) in (b), where τ and M discontinuously change.

5. Concluding remarks

In this paper we calculate only nominal stresses, however it is also interesting to calculate true stresses. Moreover, the internal variable σ can represent not only the direction of polymer but also electric dipole moment, where in the latter case the interaction between the variables σ should be polar. The simulation results corresponding to these conditions will be reported in the future.

Finally, we should like to write speculative comments. Our goal is not simply to find a model that explains rubber elasticity but to find an energy functional that accounts for the complete loading-unloading cycle of rubber, on physical-chemical basis. From this modeling basis, using mathematical tools, a constitutive function will be implemented in Finite Element software to perform 3D simulations predicting behavior under various conditions (strain rate, temperature, etc.).

Acknowledgment

This work is supported in part by JSPS KAKENHI Grant Number JP17K05149 and the Collaborative Research Project of the Institute of Fluid Science, Tohoku University.

References

[1] P.-A. Albouy, Polymer **41** (2000) 3083-3086.
[2] L. Imbernon, R. Puachet, M. Pire, P.-A. Albouy, S.Tencé-Giraut and S. Norves, Polymer **93** (2016) 189-197.
[3] N. Candau, L. Chazeau, J-M. Chenal, C. Gauthier, J. Ferreira, E. Munch, and C. Rochas, Polymer **53** (2012) 2540-2543.
[4] S. Toki et al. J. Polym. Sci. B 42 (2004) 956-964.
[5] H. Koibuchi and H. Sekino, Physica A **393** (2014) 37-50.
[6] K. Osari and H. Koibuchi, Polymer **114** (2017) 355-369.
[7] E. Proutorov, N. Matsuyama and H. Koibuchi, J. Phys. (Cond. Mat.) **30** (2018) 405101, doi.org/10.1088/1361-648X/aadcba.
[8] H. Koibuchi, Polymers **10**(7) (2018) 757(1-16).
[9] Y. Takano and H. Koibuchi, Phys. Rev. E **95** (2017) 042411(1-11).
[10] K. Mitsuhashi, S. Ghosh and H. Koibuchi, Polymers **10**(7) (2018) 715(1-18).
[11] S. Usui and H. Koibuchi, Polymers **8** (2016) 284(1-18).
[12] S. Pradhan, F.R. Costa, U. Wagenknecht, D. Jehnichen, A.K. Bhowmick, G. Heinrich, Euro. Polymer J. **44** (2008) 3122-3132.
[13] V. Shahedifar and A. M. Rezadoust, Reinforced Plastics and Composite, **32** (2013) 681-688.
[14] Y. Kawano, Y. Wang, R.A. Palmer, S.R. Aubuchon, Polimeros: Ciencia Tecnologia, **12** (2002) 96-101.